# Detection of Triacetone Triperoxide (TATP) Precursors with an Array of Sensors Based on MoS₂/RGO Composites

**Qihua Sun [1], Zhaofeng Wu [1,2,*], Haiming Duan [1,*] and Dianzeng Jia [2,*]**

[1] School of Physics Science and Technology, Xinjiang University, Urumqi 830046, China; SUNQIHUA520@163.com

[2] Key Laboratory of Energy Materials Chemistry, Ministry of Education, Key Laboratory of Advanced Functional Materials, Xinjiang University, Urumqi 830046, China

\* Correspondence: wzf911@mail.ustc.edu.cn (Z.W.); dhm@xju.edu.cn (H.D.); jdz@xju.edu.cn (D.J.)

check for updates

**Abstract:** Triacetone triperoxide (TATP) is a self-made explosive synthesized from the commonly used chemical acetone ($C_3H_6O$) and hydrogen peroxide ($H_2O_2$). As $C_3H_6O$ and $H_2O_2$ are the precursors of TATP, their detection is very important due to the high risk of the presence of TATP. In order to detect the precursors of TATP effectively, hierarchical molybdenum disulfide/reduced graphene oxide (MoS₂/RGO) composites were synthesized by a hydrothermal method, using two-dimensional reduced graphene oxide (RGO) as template. The effects of the ratio of RGO to raw materials for the synthesis of MoS₂ on the morphology, structure, and gas sensing properties of the MoS₂/RGO composites were studied. It was found that after optimization, the response to 50 ppm of $H_2O_2$ vapor was increased from 29.0% to 373.1%, achieving an increase of about 12 times. Meanwhile, all three sensors based on MoS₂/RGO composites exhibited excellent anti-interference performance to ozone with strong oxidation. Furthermore, three sensors based on MoS₂/RGO composites were fabricated into a simple sensor array, realizing discriminative detection of three target analytes in 14.5 s at room temperature. This work shows that the synergistic effect between two-dimensional RGO and MoS₂ provides new possibilities for the development of high performance sensors.

**Keywords:** (TATP) precursors; MoS₂/RGO composites; sensor arrays; synergistic effect

## 1. Introduction

The detection of explosives remains a challenge to the rapid development of modern life [1]. The detection technology of explosives requires not only simple and inexpensive constituents, but also the ability to detect specific explosives quickly and accurately. In 1895, Wolffenstein found and synthesized triacetone triperoxide (TATP) [2], which is a self-made explosive synthesized from the common chemicals acetone ($C_3H_6O$) and hydrogen peroxide ($H_2O_2$) found in daily life [3,4]. Because it is difficult to detect [5,6], it is more popular for terrorist activities [4,7–10]. Therefore, it is very important to carry out the continuous monitoring of TATP precursors ($C_3H_6O$ and $H_2O_2$) in public places [11,12]. In the past, researchers have also reported many TATP detection methods. For example, infrared (IR) [13], Raman spectroscopy [14,15], and mass spectrometry (MS) [16,17] detection methods; these detection methods have some defects of low sensitivity, slow response, high production cost, and a certain risk of detection [18,19]. In recent years, many articles on the detection of $H_2O_2$ have been reported, and their applications include environmental, biological, food, and industrial fields, using such as the non-enzymatic chemi-resistive $H_2O_2$ sensor [20,21], and reports of a $C_3H_6O$ sensor [22–24],

which achieve the advantages of low cost detection. In fact, simultaneous detection of $H_2O_2$ and $C_3H_6O$ would provide a viable basis for the detection of explosive TATP. Of course using electrochemical detection of TATP precursors is not a new concept [8,25,26]. The Vladimir [27] team introduced a good response with nano-spring-based sensors for gases such as TATP precursors, as well as determining conditions for $In_2O_3$ [28] and $WO_3$ [29] but still did not achieve operation at room temperature. The application of graphene in chemical gas sensors is receiving more and more attention [30,31]. Some important factors affecting the sensing properties of graphene were found in the process of continuous optimization of graphene sensing performances, for example, structural defects [32] and doped metal oxides [33]. Experiments [34] have shown that the defects at the edges of graphene nanoribbons interact more strongly with gas molecules, and the reduced graphene oxide (RGO) has a high defect density for fabricating gas sensors [35]. The composite materials based on RGO and metal oxides have been widely used for gas sensing, $RGO/Fe_2O_3$ nanocomposites achieve high selectivity to $NO_2$ at room temperature and $RGO/SnO_2$ etc. achieve detection of ambient gases at room temperature. Based on these experiments, it is necessary to achieve high sensitivity, rapid response, and accurate identification detection of TATP precursor gas at room temperature. It can be seen that RGO-based composite materials provide hope for the sensitive detection of TATP precursors at room temperature. More recently, composite materials of $RGO/MoS_2$ have been fabricated and proved to be effective in gas sensing performance. The Bon-Cheol Ku team reported that the $MoS_2/RGO$ composite film can be used as a highly sensitive gas sensor that can detect concentrations of harmful gases such as $NO_2$ as low as 0.15 ppm [35]. It is reported that the $RGO/MoS_2$ hybrid film not only shows improved sensitivity to $CH_2O$ at room temperature, but also exhibits fast response characteristics and good reproducibility [36].

Both RGO and $MoS_2$ are typical two-dimensional nanomaterials, which are generally p-type and n-type semiconductors, respectively [37,38]. As far as we know, $RGO/MoS_2$ composites have not been used to detect TATP precursors sensitively at room temperature. The synergistic effect of RGO and $MoS_2$ in gas sensing detection of TATP precursors is worth studying. Inspired by the above researches, in order to detect precursors of TATP effectively, the hierarchical $MoS_2/RGO$ composites were synthesized by a hydrothermal method, using two-dimensional RGO as template. The effects of the ratio of RGO to raw materials for the synthesis of $MoS_2$ on the morphology, structure, and gas sensing properties of the $MoS_2/RGO$ composites were studied.

## 2. Materials and Methods

### 2.1. Preparation of MoS₂/RGO Composites

Ammonium molybdate [$(NH_4)_6Mo_7O_{24}\cdot4H_2O$], thiourea ($CH_4N_2S$), and ethanol ($C_2H_6O$), analytical reagents, were purchased from Sinopharm Chemical Reagent Co., Ltd. $H_2O_2$ (30%) was purchased from Aladdin Reagent Co., Ltd. Graphene Oxide (GO) was synthesized from natural flake graphite (100 mesh) by Hummers method [39,40]. The preparation process of the $MoS_2/RGO$ composites can be summarized as follows. Amounts of, 1, 0.5, 0.33 mmol $(NH_4)_6Mo_7O_{24}\cdot4H_2O$ and 30, 15, 10 mmol $CH_4N_2S$ were dissolved in 35 mL diluted graphene solution, respectively, and stirred for 30 min to make them homogeneous. The three solutions were then transferred into three 45 mL polytetrafluoroethylene (PTFE) stainless steel autoclaves and maintained at 180 °C for 24 h. As shown in Figure 1, the raw materials for synthesis of $MoS_2$ adsorbed on RGO first nucleate at high temperature to form $MoS_2$ nanocrystals, and then form $MoS_2/RGO$ composites. Finally, the reaction system was cooled to room temperature naturally, the product was collected by centrifugation, washed with deionized water, and the sample preparation was concluded after drying for 20 h at 70 °C. For the convenience of description, the $MoS_2/RGO$ composites from 1, 0.5, 0.33 mmol $(NH_4)_6Mo_7O_{24}\cdot4H_2O$ and 30, 15, 10 mmol $CH_4N_2S$ were designated as $MoS_2/RGO-1$, $MoS_2/RGO-2$ and $MoS_2/RGO-3$.

**Figure 1.** Schematic diagram of MoS$_2$/RGO composite with reduced graphene oxide (RGO) as template.

## 2.2. Characterization

The crystal structure of MoS$_2$/RGO was characterized by X-ray diffraction (XRD) (Bruker D8 Advance, with Cu-K$_\alpha$ radiation). The morphology of MoS$_2$/RGO was observed by transmission electron microscopy (TEM, JEM-2100F, Japan) and field emission scanning electron microscopy (FE-SEM, S-4800, Hitachi, Japan). The surface properties of MoS$_2$/RGO were recorded using a Fourier Transform Infrared (FT-IR) spectrometer (Bruker-V Vertex 70, Karlsruhe, Germany). Raman Detection of samples was with a Raman Spectrometer (Raman spectrometer, Horiba Company, iHR550, Shanghai, China). The chemical composition of the main elements was studied by X-ray photoelectron spectroscopy (XPS K-Alpha+, Thermo Fisher Scientific, Waltham, MA, USA). The I–V curves of the sensors were tested by an electrochemical workstation (CIMPS-2, ZAHER ENNIUM) at room temperature.

## 2.3. Manufacture and Testing of Sensor Parts

The blank sensor chip was purchased from Beijing Elite Co., Ltd., Beijing, China. Platinum interdigitated electrodes with both finger-width and interfinger spacing of about 200 μM were printed on a ceramic substrate, forming a blank sensor chip. First, the sample was mixed with a quantity of deionized water to form a uniform slurry, and then the platinum finger fork electrode used to apply the uniform slurry to the ceramic substrate while the sensing film was formed by drying at room temperature (25 °C) for 24 h. The sensors based on MoS$_2$/RGO-1, MoS$_2$/RGO-2, and MoS$_2$/RGO-3 were designated as sensor 1, sensor 2, and sensor 3, respectively. Finally, the sensor was aged in air for about 24 h with a 0.5 V voltage to ensure good stability. The gas sensing tests, including the definition of response, response time, and recovery time in this work are similar to the previous report [41]. The specific sensing tests of H$_2$O$_2$, C$_3$H6O, C$_2$H$_6$O vapors, and Ozone (O$_3$) are shown in the Supplementary Figure S1, and the sensitivity data was recorded by an electrochemical workstation (CIMPS-2, ZAHER ENNIUM) in a 25 °C air-conditioned room.

## 3. Results and Discussion

### 3.1. Characterization Results of MoS$_2$/RGO

Figure 2a–f shows the scanning electron microscope (SEM) images of the obtained MoS$_2$/RGO composites. It can be seen from the graph that the evolution of the morphology structure of the composites varies with the ratio of RGO to raw materials for the synthesis of MoS$_2$. The raw materials for synthesis of MoS$_2$ adsorbed on RGO first nucleate at high temperature to form MoS$_2$ nanocrystals, and then form MoS$_2$/RGO composites. Evidently, for the MoS$_2$/RGO-1 and MoS$_2$/RGO-2 composites, RGO was relatively small relative to MoS$_2$, which was almost completely coated by the excess of MoS$_2$ (Figure 2a–d). In the precursor mixed solution of MoS$_2$/RGO-1 of MoS$_2$/RGO-3, the content of RGO remained unchanged, while the ratio of ammonium molybdate and thiourea decreased gradually. For the MoS$_2$/RGO-3 composites, the amount of raw materials

$((NH_4)_6Mo_7O_{24} \cdot 4H_2O$ and $CH_4N_2S)$ for the synthesis of $MoS_2$ is only one third of that for $MoS_2/RGO$-1 composites. For the $MoS_2/RGO$-1 and $MoS_2/RGO$-2, the concentrations of $(NH_4)_6Mo_7O_{24} \cdot 4H_2O$ and $CH_4N_2S$ are higher, so the nucleation rate and growth rate are faster than that of $MoS_2/RGO$-3. As a result, $MoS_2/RGO$-1 and $MoS_2/RGO$-2 grow rapidly into small grains (Figure 2a–d). In contrast, the nucleation rates and growth rate of $MoS_2/RGO$-3 are slower because of its lower concentration, and it grows into a finer pattern structure (Figure 2e,f). Therefore, $MoS_2$ can grow well with RGO as template, and finally form the hierarchical $MoS_2/RGO$-3 composites (Figure 2e,f). As shown in Figure 2e,f, the $MoS_2/RGO$-3 composites eventually form interconnected, patterned spheres and the thickness of the curved pattern $MoS_2$ sheet is only about 20 nm. The hierarchical structure, ultra-thin thickness provides sufficient channels and sites for the adsorption and desorption of the target gas, which is helpful to improve the sensitivity of the sensor and the speed of adsorption and desorption.
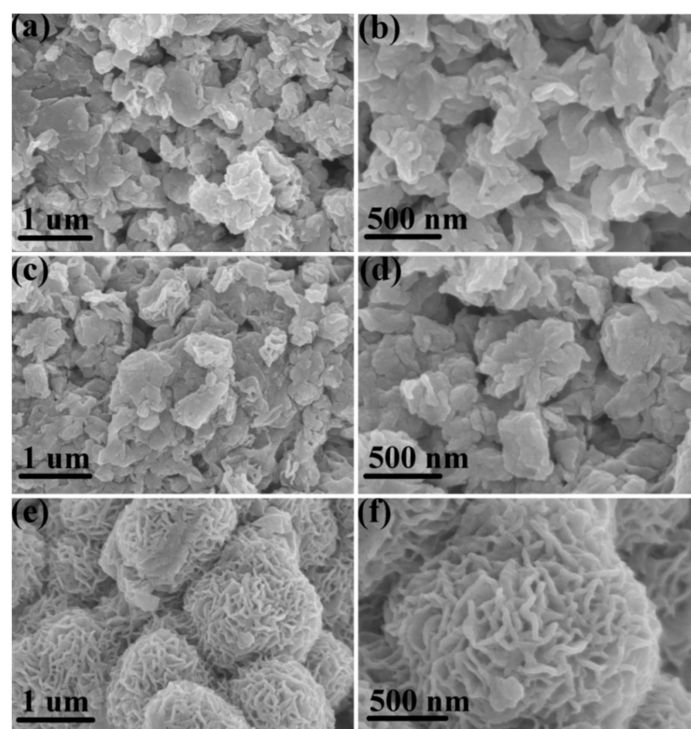


**Figure 2.** SEM images of (**a**,**b**) $MoS_2/RGO$-1, (**c**,**d**) $MoS_2/RGO$-2, and (**e**,**f**) $MoS_2/RGO$-3 composites.

X-ray diffraction (XRD) analysis was performed on $MoS_2/RGO$-1, $MoS_2/RGO$-2, and $MoS_2/RGO$-3 composites to examine the crystal structure. As shown in Figure 3a, the diffraction peak at $2\theta = 28.5°$ is sharp, and the sharpness becomes larger as the ratio changes, indicating that the crystallinity of the sample is constantly improving [42]. In addition, the position of the peak is also shifted to the left, indicating that the lattice size has changed, this result is consistent with the measured results of the SEM. It is noteworthy that the absence of high-indexed diffraction peaks indicates short-range disordering nature in the products, which may offer more active sites for gas sensing [41]. To determine the functional groups contained in the samples, FT-IR analysis was performed and is shown in Figure 3b. Due to the presence of hydroxyl groups (–OH), the $MoS_2/RGO$ samples showed 3140 $cm^{-1}$ and 3428 $cm^{-1}$ peaks in the range of 3000–3800 $cm^{-1}$, respectively [43]. The absorption peak at 1624 $cm^{-1}$ is related to the in-plane vibration of the H–O–H bending band of the adsorbed $H_2O$ molecule or the C–C bonding of the $sp^2$ hybrid, 1400 $cm^{-1}$ (carboxy O–H stretching) [44], and 1031 $cm^{-1}$ (C–O) [43]. Because RGO was not observed in the SEM images, Raman spectroscopy was performed to determine the composition of the composites (Figure 3c). The Raman spectra of the composites shown at 1305 $cm^{-1}$ and 1542 $cm^{-1}$ correspond to the D,

G bands of RGO, respectively. The G band is produced by the surface vibration of the sp$^2$ carbon atom, which is consistent with the results of the FT-IR test while the D band is usually considered to be the disordered vibration peak of graphene [45,46]. These results prove the existence of RGO in the composites. I–V characteristic curves of the sensors based on $MoS_2$/RGO composites also were performed to prove the existence and function of RGO in the $MoS_2$/RGO composites (Figure 3d). The linear I–V relations showed a perfect ohmic contact between $MoS_2$/RGO composites and the metal electrode [47,48]. Compared with $MoS_2$, RGO has the better conductivity. Therefore, with the increase of RGO proportion in the composites, the conductivity increases from $MoS_2$/RGO-1 to $MoS_2$/RGO-3, which also proves the existence and function of RGO in the composites. The existence of RGO was also demonstrated by direct TEM observations. As shown in Figure 3e,f, TEM images of the $MoS_2$/RGO composite shows the wrinkled RGO and the $MoS_2$ anchored on RGO. The $MoS_2$/RGO composite provides nanoscale $MoS_2$ flakes in the form of loose agglomerates on RGO, which can also be distinguished by their brightness. As shown by the yellow lines in the Figure 3f, one can directly observe the crystalline interplanar spacing attributed to $MoS_2$, and the average interplanar spacing from the six spacing was calculated to be 0.63 nm. The 0.63 nm of interplanar spacing was attributed to the (002) planes of $MoS_2$ [45], proving the existence of the $MoS_2$ anchored on RGO. These observations are consistent with the Raman results, indicating the successful preparation of $MoS_2$/RGO composites.
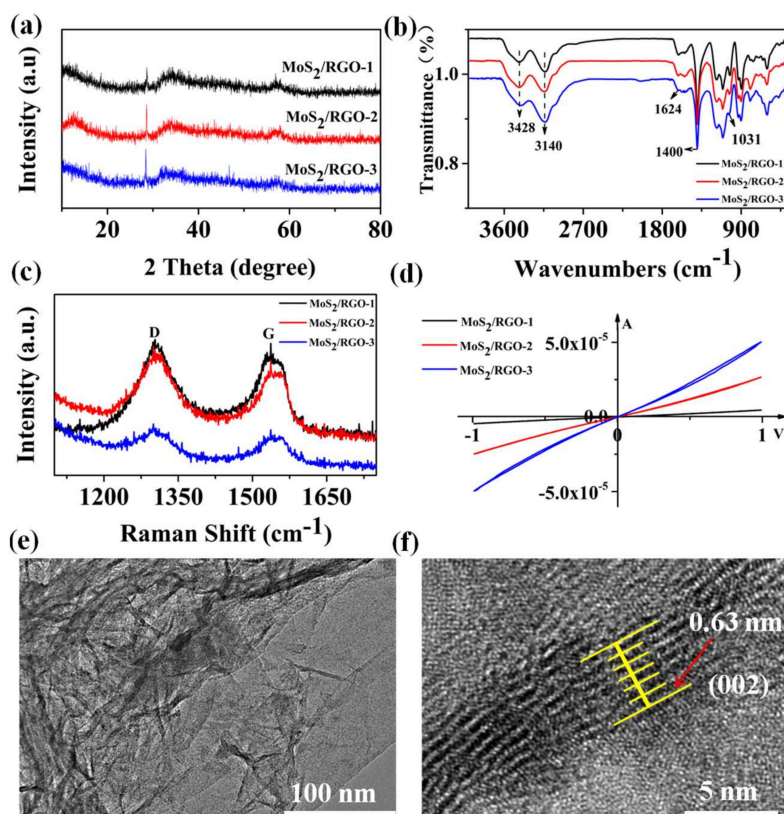


**Figure 3.** (**a**) XRD patterns, (**b**) FT-IR spectrum, (**c**) Raman spectrum of $MoS_2$/RGO-1, $MoS_2$/RGO-2, and $MoS_2$/RGO-3 composites; (**d**) I–V curves of sensors 1, 2, 3 and (**e**,**f**) TEM images of $MoS_2$/RGO-3 composites.

In order to further confirm the distribution of the elements contained in the composites, the chemical states of the $MoS_2$/RGO composite were investigated by XPS. Figure 4a shows that the main constituent elements in the $MoS_2$/RGO composites are S, Mo, C, and O. The high-resolution Mo3d spectrum shows two distinct peaks at 227.86 and 231.12 eV, corresponding to Mo3d$_{5/2}$ and Mo3d$_{3/2}$, respectively (Figure 4d). The binding energies of 160.81 and 161.9 eV correspond to S2p$_{3/2}$ and S2p$_{1/2}$, respectively [49] (Figure 4e). One can see intuitively from the Figure 4b–e that except for C,

the corresponding peaks of S, Mo, and O are reduced from the $MoS_2/RGO-1$ to $MoS_2/RGO-3$, which is consistent with the increasing proportion of RGO in the composites. It is worth noting that with the increasing proportion of RGO in the composites, the intensity ratio of C1s to S2p increases gradually (Figure 4f). This normalized result is consistent with the previous characterization analysis, demonstrating that the ratio of RGO to raw materials for synthesis of $MoS_2$ effectively influences the components, morphology, and structures of the $MoS_2/RGO$ composites. One can expect that these changes will also have a significant impact on the gas sensitivity of $MoS_2/RGO$ composites [50].
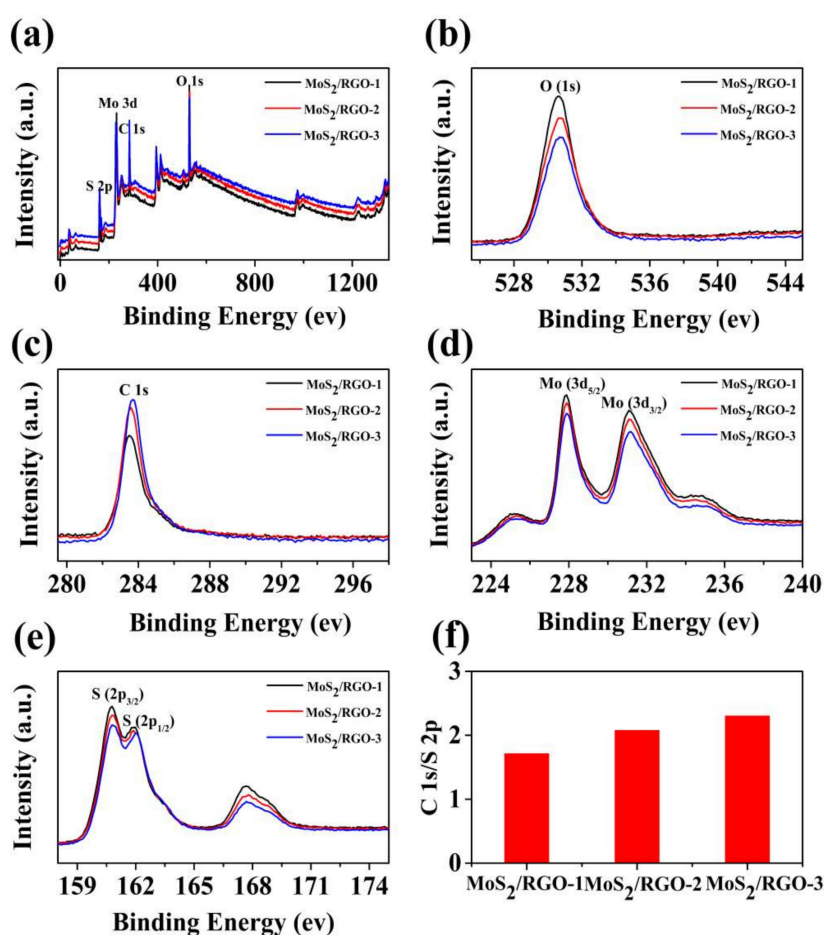


**Figure 4.** XPS spectra of $MoS_2/RGO$ composites (**a**) high-resolution spectra, (**b**) O1s (**c**) C1s, (**d**) Mo3d, (**e**) S2p, and (**f**) ratio of the intensity of C1s to S2p.

### 3.2. Fabrication and Testing of Sensor Array

Figure 5a shows the dynamic sensing curves of the sensors based on different samples at room temperature to 50 ppm of $H_2O_2$, $C_3H_6O$, and $C_2H_6O$ vapors. As can be clearly seen from the sensing curves, the three sensors based on $MoS_2/RGO$ composites respond upward to oxidizing $H_2O_2$ vapor and downward to reducing $C_3H_6O$ and $C_2H_6O$ vapors, reflecting the sensing characteristics of p-type semiconductors. Generally, RGO and $MoS_2$ are p-type and n-type semiconductors, respectively. The p-type sensing characteristics prove that RGO plays an important role in gas sensing of $MoS_2/RGO$ composites. It is worth noting that the responses of the three sensors based on $MoS_2/RGO$ composites to 50 ppm of $H_2O_2$, $C_3H_6O$, and $C_2H_6O$ vapors increases with the increase of RGO content (Figure 5b). The responses to 50 ppm of $H_2O_2$ vapor increased from 29.0% to 59.6%, and then to 373.1% for the sensors 1, 2, and 3, respectively. This trend of responses also applies to 50 ppm of $C_2H_6O$ vapor, but not $C_3H_6O$ vapor. This phenomenon can be attributed to the charge depletion layer and hierarchical structures. It is well known that both the charge depletion layer and the particle

size of the semiconductor materials determine the sensing performance of the chemi-resitive sensor. The higher the proportion of the electron depletion layer in the semiconductor particle, the better the gas sensitivity of the sensing materials. The $MoS_2$/RGO-3 composite has a pattern-like hierarchical structure with a thickness of about 20 nm, and target gas molecules can be adsorbed on both sides of the sheet structures to form a deeper charge depletion layer. In addition, the hierarchical structure of $MoS_2$/RGO-3 composite provides a larger specific surface area and more active sites. As a result, the deeper charge depletion layer, larger specific surface area, and more active sites of the $MoS_2$/RGO-3 composite contributed to the higher sensitivity, which is consistent with the results of the gas sensitivity test. In contrast, pure $MoS_2$ was also prepared, and their two-dimensional sheet morphologies are shown in Figure S2a–f. The sensing curves of sensors based on pure $MoS_2$ and RGO to 1000 ppm of $H_2O_2$, $C_3H_6O$, and $C_2H_6O$ vapors were also tested (Figure S3a). It can be seen from the Figure S3b–d that although the concentration of $H_2O_2$, $C_3H_6O$, and $C_2H_6O$ vapors increased 20 times (1000 ppm), the corresponding responses of the sensors based on pure $MoS_2$ and RGO hardly increased significantly compared with the responses of the sensors based on $MoS_2$/RGO composites to 50 ppm of $H_2O_2$, $C_3H_6O$, and $C_2H_6O$ vapors. This fully illustrates the important role of the synergistic effect of $MoS_2$ and RGO in gas sensing. In addition, for the three target gases, all three sensors based on $MoS_2$/RGO composites show very short response time and recovery time, reflecting the fast adsorption and desorption of target gases on the surface of $MoS_2$/RGO composites. As shown in Figure 5c, the maximum response time and recovery time are no more than 14.5 s and 16.3 s, respectively, proving the real-time sensing performance of the sensors. For an excellent gas sensor, not only is high response required in practical applications, but also good selectivity to the target gas. $C_2H_6O$ is a common volatile organic compound that interferes greatly with the detection of TATP precursors, it is very necessary to use $C_2H_6O$ vapor as an interference factor in the detection of TATP precursors. Unfortunately, the $MoS_2$/RGO-3 composite has a higher response to $C_2H_6O$ vapor than that of $C_3H_6O$ vapor (Figure 5a,b), showing the poor anti-interference characteristics to $C_2H_6O$ vapor. Moreover, $O_3$ is a strong oxidizing gas in the air and $O_3$ often interferes with the sensing detection of oxidizing gases. Therefore, we also tested the sensors based on $MoS_2$/RGO composites to 50 ppm of $O_3$ gas (Supplementary Figure S4). It can be seen from Figure S4 that the sensors based on $MoS_2$/RGO composites hardly respond to 50 ppm of $O_3$, showing good anti-interference ability of $O_3$.
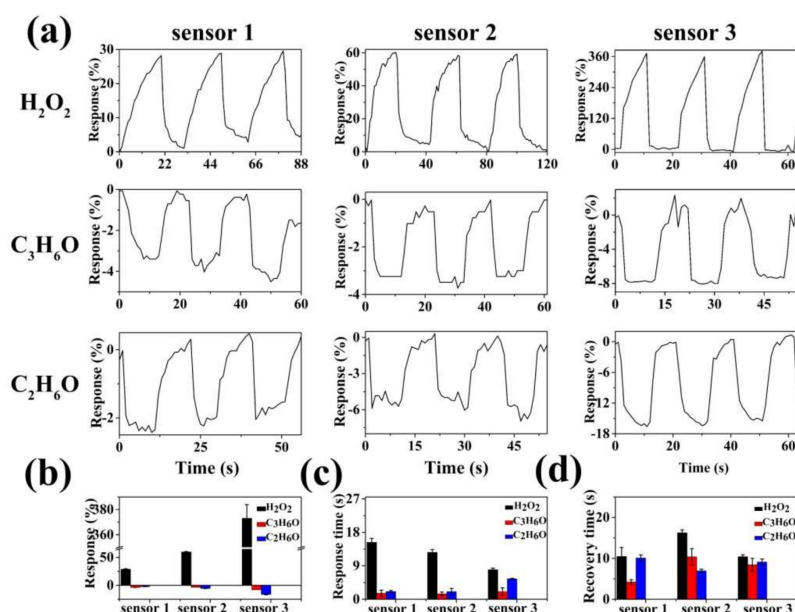


**Figure 5.** (**a**) Dynamic sensing curves of the devices based on sensor 1, 2, and 3 to 50 ppm of $H_2O_2$, $C_3H_6O$, $C_2H_6O$ vapors at room temperature; statistical graph of (**b**) average response, (**c**) response time and (**d**) recovery time corresponding to the sensing curves.

The sensing performances of sensors based on $MoS_2/RGO$-3 and other reported chemi-resistive sensors for detection of $H_2O_2$ vapor can be found in Table 1. As can be seen clearly from the Table 1, our sensors also work at room temperature like the reported sensors, but the sensor in our work has the highest sensitivity to $H_2O_2$ vapor at room temperature, achieving a response of 373.1% to 50 ppm $H_2O_2$ vapor. The response time for 50 ppm $H_2O_2$ vapor is approximately 9 s. This comparison shows that our sensor of $MoS_2/RGO$-3 has better comprehensive sensing performance for $H_2O_2$ vapor.

**Table 1.** Comparison of the reported $H_2O_2$ sensors and our sensors of $MoS_2/RGO$-3.

| Sensing Materials | Analyte Concentration | Temperature (°C) | Response (%) | Response Time | Ref. |
|---|---|---|---|---|---|
| SWCNTs | 100 ppm $H_2O_2$ | 25 | ~1.97 | ~20 s | [51] |
| Pt-SWCNTs | 60.6 ppm $H_2O_2$ | 23 ± 1 | ~50 | ~240 s | [52] |
| CuPc-f-MWNTs | | | (−) 24.2 | 2 s | |
| CoPc-f-MWNTs | 34% $H_2O_2$ (aq) vapors | Ambient temperature | (+) 3.8 | 2 s | [53] |
| VPc-f-MWNTs | | | (−) 4.4 | 4 s | |
| $MoS_2/RGO$-3 | 50 ppm $H_2O_2$ | 25 | ~373.1 | ~9 s | This work |

In addition, the response of the $MoS_2/RGO$-3 sensor to different concentrations of $H_2O_2$ vapor was tested (Figure 6a). Based on the results, the estimated detection limit (defined as the detection limit = $3S_D/m$, where m is the slope of the linear portion of the calibration curve, $S_D$ is the standard deviation of the noise in the response curve) [41], and the $H_2O_2$ vapor is determined to be 0.65 ppm (Figure 6b). The results show that $MoS_2/RGO$-3 composites have potential applications of gas detection of TATP precursors.
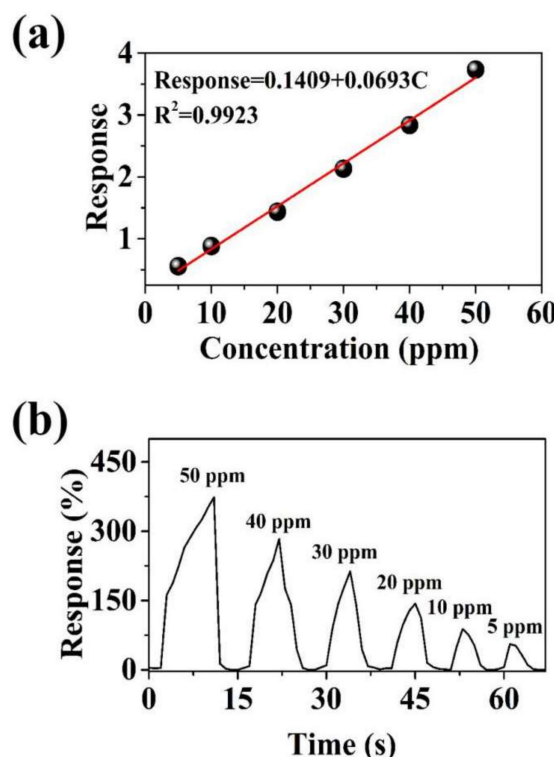


**Figure 6.** (**a**) Response curves of $MoS_2/RGO$-3 sensor to different concentrations of $H_2O_2$ vapor and (**b**) plots of the fitting of response vs concentration.

## 3.3. Discriminative Capability of the Sensor Array

To evaluate the discriminative capability of a simple array consisting of three sensors, all the responses were further analyzed using a principal component analysis (PCA) method

and radar method combining kinetic and thermodynamic parameters. The kinetic and thermodynamic parameters of the interaction of the analytes and the sensor array are utilized to assess the discriminative capability of the sensor array. The radar method refers to fingerprint recognition, which creates a unique database of explosive fingerprints, enabling the separation of similar chemical entities and providing a fast and reliable method for identifying individual chemical reagents [54,55]. The responses and response time inherent in the interaction between each analyte and the three sensors were chosen as kinematic and thermodynamic parameters, respectively. Therefore, its three pairs of sensing responses and response times from the sensor array were used to calculate the ratio of responses to response times, and the three parameters obtained for each analyte represent the fingerprint. From the fingerprints obtained (Figure 7a–c), one can see that the triangular fingerprints corresponding to $H_2O_2$, $C_3H_6O$, and $C_2H_6O$ vapors are not well differentiated because the number of sensors is too small. Therefore, the PCA method is used to evaluate the discriminative ability of the sensor array. PCA is a popular multivariate statistical technique used to simplify data sets. The purpose of this method is to reduce the dimension of multivariate data while retaining as much relevant information as possible [56,57]. Data sets of principal component analysis applied to pattern recognition and/or gas recognition have been reported [58]. As shown in Figure 7d, it can be clearly seen that the simple sensor array is very effective in distinguishing three target analytes, showing the discriminative capability. It also proves that the design of gas sensing properties of $MoS_2$/RGO composites by changing the ratio of RGO to $MoS_2$ is effective and feasible. Considering that the maximum response time of the sensor array is just 14.5 s, means that the simple sensor array can detect three analytes in 14.5 s.
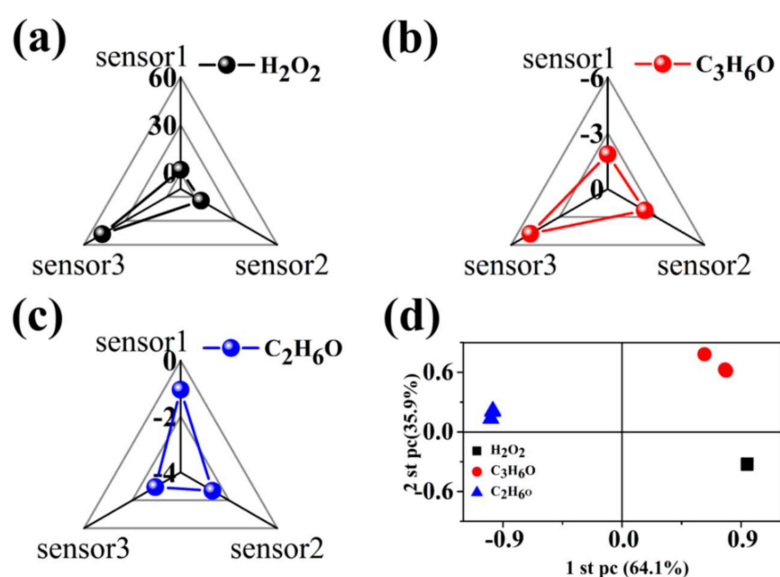


**Figure 7.** Fingerprints combining kinetic and thermodynamic parameters of (**a**) $H_2O_2$, (**b**) $C_3H_6O$, (**c**) $C_2H_6O$; (**d**) Two-dimensional principal component analysis (PCA) plots according to the responses to $H_2O_2$, $C_3H_6O$, and $C_2H_6O$ of sensor array.

### 3.4. Analysis of the Possible Sensing Mechanism

The conductivity of the sensing material depends on the adsorbed gas molecules (oxidizing or reducing) [59]. Generally, $MoS_2$ acts as an n-type semiconductor [37,38], while RGO is considered to be a p-type semiconductor with a defect site and a functionalized group on its surface, which acts as an active site for the gas, facilitating the adsorption of gas molecules [60]. The gas sensing results show that the $MoS_2$/RGO composite exhibits the characteristics of p-type semiconductors.

When the sensors based on $MoS_2$/RGO composites were exposed to the reducing $C_3H_6O$ vapor, the following reactions occurred.

$$C_3H_6O \text{ (g)} + 4O_2^- \text{ (s)} \rightarrow 3CO_2 + 3H_2O + 4e^- \tag{1}$$
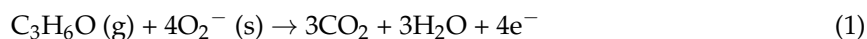
According to Equation (1), $MoS_2$/RGO composites captured the electrons from the reducing $C_3H_6O$ vapor, while the conductivity of composites decreases, exhibiting characteristics of p-type semiconductors. It is reported that $H_2O_2$ will react in the following two ways depending on the concentration of hydrogen peroxide. At high $H_2O_2$ (of about 10 vol%) concentrations the mechanism is as follows [61]:

$$2H_2O_2 \rightarrow 2H_2O + O_2 \tag{2}$$

At lower concentrations (2.1 vol%) the net reaction is:

$$2H_2O_2 \rightarrow 2H_2O + 0.87O_2 + 0.08O_3 \tag{3}$$

In our work, $H_2O_2$ with a mass fraction of 30% was used. According to Equation (2), the main product of $H_2O_2$ decomposition is $O_2$. Therefore, the produced $O_2$ and $H_2O_2$ vapor will capture electrons from the $MoS_2$/RGO composites, and the conductivity of the composites increases, also exhibiting characteristics of p-type semiconductors. This indicated that RGO played an important role in the gas sensing properties of $MoS_2$/RGO composites. Because RGO/$MoS_2$ conjugates can form excellent charge transfer pathways [45], the charge can favorably travel from $MoS_2$ to RGO quickly, resulting in a very large and fast variation of the conductivity. This synergy of $MoS_2$ and RGO contributes to a quick and sensitive response to target analytes. With the decrease of $MoS_2$ (or the increase of RGO) in the RGO/$MoS_2$ composite, the contact between RGO and $MoS_2$ is more sufficient, which is more conducive to giving a good gas sensing performance. Therefore, the sensitivity of the sensor based on $MoS_2$/RGO composites was significantly improved with the increase of RGO within an appropriate range. Without doubt, the formation of hierarchical structure of the $MoS_2$/RGO composites is also conducive to improving sensitivity, which is consistent with the very good sensitivity of sensor-3 of $MoS_2$/RGO composites.

## 4. Conclusions

p-type RGO and n-type $MoS_2$, typical two-dimensional nanomaterials, were used successfully to design hierarchical $MoS_2$/RGO composites using RGO as templates. The effects of the ratio of RGO to raw materials for the synthesis of $MoS_2$ on the morphology, structure, and gas sensing properties of the $MoS_2$/RGO composites were studied in order to detect the precursors of TATP effectively. It was found that after optimization, the response to 50 ppm of $H_2O_2$ vapor was increased from 29.0% to 373.1%, achieving an increase of about 12 times. Meanwhile, all three sensors based on $MoS_2$/RGO composites exhibited excellent anti-interference performance to ozone with strong oxidation. Furthermore, the simple sensor array based on $MoS_2$/RGO composites achieved discriminative detection of three target analytes in 14.5 s at room temperature. This proves that the design of gas sensing properties of $MoS_2$/RGO composites by changing the ratio of RGO to $MoS_2$ is effective and feasible. The synergistic effect between two-dimensional RGO and $MoS_2$ provide new possibilities for the development of high performance sensors.

**Author Contributions:** Z.W., D.J. and H.D. conceived and designed the experiments; Q.S. and Z.W. performed the experiments; Q.S., Z.W., D.J., and H.D. analyzed the data and wrote the paper.

**Conflicts of Interest:** The authors declare no conflict of interest

## References

1. Suman, P.; Wujian, M. Sensitive determination of triacetone triperoxide explosives using electrogenerated chemiluminescence. *Anal. Chem.* **2013**, *85*, 8008–8015.
2. Beveridge, A. *Forensic Investigation of Explosions*; CRC Press: Boca Raton, FL, USA, 1998.
3. Capua, E.; Cao, R.; Sukenik, C.N.; Naaman, R. Detection of triacetone triperoxide (TATP) with an array of sensors based on non-specific interactions. *Sens. Actuators B Chem.* **2009**, *140*, 122–127. [CrossRef]
4. Dubnikova, F.; Kosloff, R.; Zeiri, Y.; Karpas, Z. Novel Approach to the Detection of Triacetone Triperoxide (TATP): Its Structure and Its Complexes with Ions. *Phys. Chem. A* **2002**, *106*, 4951–4956. [CrossRef]
5. Muller, D.; Levy, A.; Shelef, R.; Abramovich-Bar, S.; Sonenfeld, D.; Tamiri, T. Improved method for the detection of TATP after explosion. *J. Forensic Sci.* **2004**, *49*, 935–938. [CrossRef]
6. Oxley, J.C.; Smith, J.L.; Shinde, K.; Moran, J. Determination of the Vapor Density of Triacetone Triperoxide (TATP) Using a Gas Chromatography Headspace Technique. *Propellants Explos. Pyrotech.* **2010**, *30*, 127–130. [CrossRef]
7. Mamo, S.K.; Gonzalez-Rodriguez, J. Development of a molecularly imprinted polymer-based sensor for the electrochemical determination of triacetone triperoxide (TATP). *Sensors* **2014**, *14*, 23269–23282. [CrossRef]
8. Hengwei, L.; Suslick, K.S. A colorimetric sensor array for detection of triacetone triperoxide vapor. *J. Am. Chem. Soc.* **2010**, *132*, 15519–15521.
9. Fan, W.; Young, M.; Canino, J.; Smith, J.; Oxley, J.; Almirall, J.R. Fast detection of triacetone triperoxide (TATP) from headspace using planar solid-phase microextraction (PSPME) coupled to an IMS detector. *Anal. Bioanal. Chem.* **2012**, *403*, 401–408. [CrossRef] [PubMed]
10. Jiang, D.; Peng, L.; Wen, M.; Zhou, Q.; Chen, C.; Wang, X.; Chen, W.; Li, H. Dopant-Assisted Positive Photoionization Ion Mobility Spectrometry Coupled with Time-Resolved Thermal Desorption for on-site Detection of TATP and HMTD in Complex Matrices. *Anal. Chem.* **2016**, *88*, 4391–4399. [CrossRef]
11. Lubczyk, D.; Siering, C.; Lörgen, J.; Shifrina, Z.B.; Müllen, K.; Waldvogel, S.R. Simple and sensitive online detection of triacetone triperoxide explosive. *Sens. Actuators B Chem.* **2010**, *143*, 561–566. [CrossRef]
12. Burks, R.M.; Hage, D.S. Current trends in the detection of peroxide-based explosives. *Anal. Bioanal. Chem.* **2009**, *395*, 301–313. [CrossRef] [PubMed]
13. Buttigieg, G.A.; Knight, A.K.; Denson, S.; Pommier, C.; Denton, M.B. Characterization of the explosive tricetone triperoxide and detection by ion mobility spectrometry. *Forensic Sci. Int.* **2003**, *135*, 53–59. [CrossRef]
14. Salb, C.; Wackerbarth, H.; Christou, K.; Gundrum, L.; Niederkrüger, M.; Beushausen, V.; Viöl, W. Detection of explosives based on surface-enhanced Raman spectroscopy. *Appl. Opt.* **2010**, *49*, 4362–4366.
15. Leo, W.; Stuart, W.; Konrad, S.; Andrew, C. Development of an LC/MS method for the trace analysis of triacetone triperoxide (TATP). *Analyst* **2002**, *127*, 1627–1632.
16. Zitrin, S. Decomposition products of petn in post explosion analysis. *J. Energ. Mater.* **1986**, *4*, 77–91.
17. Fang, X.; Ahmad, S.R. Detection of explosive vapour using surface-enhanced Raman spectroscopy. *Appl. Phys. B* **2009**, *97*, 723–726. [CrossRef]
18. Cotte-Rodríguez, I.; Chen, H.; Cooks, R.G. Rapid trace detection of triacetone triperoxide (TATP) by complexation reactions during desorption electrospray ionization. *Chem. Commun.* **2006**, *9*, 953–955. [CrossRef]
19. Li, X.; Zhang, Z.; Tao, L. A novel array of chemiluminescence sensors for sensitive, rapid and high-throughput detection of explosive triacetone triperoxide at the scene. *Biosens. Bioelectron.* **2013**, *47*, 356–360. [CrossRef] [PubMed]
20. Song, M.J.; Hwang, S.W.; Whang, D. Non-enzymatic electrochemical CuO nanoflowers sensor for hydrogen peroxide detection. *Talanta* **2010**, *80*, 1648–1652. [CrossRef]

21. Luo, L.; Li, F.; Zhu, L.; Zhang, Z.; Ding, Y.; Deng, D. Non-enzymatic hydrogen peroxide sensor based on $MnO_2$-ordered mesoporous carbon composite modified electrode. *Electrochim. Acta* **2012**, *77*, 179–183. [CrossRef]

22. Shen, J.-Y.; Wang, M.-D.; Wang, Y.-F.; Hu, J.-Y.; Zhu, Y.; Zhang, Y.X.; Li, Z.-J.; Yao, H.-C. Iron and carbon codoped $WO_3$ with hierarchical walnut-like microstructure for highly sensitive and selective acetone sensor. *Sens. Actuators B Chem.* **2018**, *256*, 27–37. [CrossRef]

23. Osica, I.; Imamura, G.; Shiba, K.; Ji, Q.; Shrestha, L.K.; Hill, J.P.; Kurzydlowski, K.J.; Yoshikawa, G.; Ariga, K. Highly Networked Capsular Silica-Porphyrin Hybrid Nanostructures as Efficient Materials for Acetone Vapor Sensing. *ACS Appl. Mater. Interfaces* **2017**, *9*, 9945–9954. [CrossRef]

24. Jeong, Y.J.; Koo, W.T.; Jang, J.S.; Kim, D.H.; Kim, M.H.; Kim, I.D. Nanoscale $PtO_2$ Catalysts-Loaded $SnO_2$ Multichannel Nanofibers toward Highly Sensitive Acetone Sensor. *ACS Appl. Mater. Interfaces* **2018**, *10*, 2016–2025. [CrossRef]

25. Donglai, L.; Avi, C.; Munoz, R.A.A.; Tanin, T.; Joseph, W. Highly sensitive electrochemical detection of trace liquid peroxide explosives at a Prussian-blue 'artificial-peroxidase' modified electrode. *Analyst* **2006**, *131*, 1279–1281.

26. Xie, Y.; Cheng, I.F. Selective and rapid detection of triacetone triperoxide by double-step chronoamperometry. *Microchem. J.* **2010**, *94*, 166–170. [CrossRef]

27. Dobrokhotov, V.; Oakes, L.; Sowell, D.; Larin, A.; Hall, J.; Kengne, A.; Bakharev, P.; Corti, G.; Cantrell, T.; Prakash, T. Toward the nanospring-based artificial olfactory system for trace-detection of flammable and explosive vapors. *Sens. Actuators B Chem.* **2012**, *168*, 138–148. [CrossRef]

28. Zhang, W.H.; Zhang, W.D.; Chen, L.Y. Highly sensitive detection of explosive triacetone triperoxide by an $In_2O_3$ sensor. *Nanotechnology* **2010**, *21*, 315502. [CrossRef]

29. Warmer, J.; Wagner, P.; Schöning, M.J.; Kaul, P. Detection of triacetone triperoxide using temperature cycled metal-oxide semiconductor gas sensors: Detection of triacetone triperoxide. *Phys. Status Solidi A Appl. Mater. Sci.* **2015**, *212*, 1289–1298. [CrossRef]

30. Fowler, J.D.; Allen, M.J.; Tung, V.C.; Yang, Y.; Kaner, R.B.; Weiller, B.H. Practical Chemical Sensors from Chemically Derived Graphene. *ACS Nano* **2009**, *3*, 301–306. [CrossRef]

31. Yuan, W.; Shi, G. Graphene-based gas sensors. *J. Mater. Chem. A* **2013**, *1*, 10078–10091. [CrossRef]

32. Huang, B.; Li, Z.; Liu, Z.; Zhou, G.; Hao, S.; Wu, J.; Gu, B.L.; Duan, W. Adsorption of Gas Molecules on Graphene Nanoribbons and Its Implication for Nanoscale Molecule Sensor. *J. Phys. Chem. C* **2008**, *112*, 13442–13446. [CrossRef]

33. Mao, S.; Cui, S.; Lu, G.; Yu, K.; Wen, Z.; Chen, J. Tuning gas-sensing properties of reduced graphene oxide using tin oxide nanocrystals. *J. Mater. Chem.* **2012**, *22*, 11009–11013. [CrossRef]

34. Vedala, H.; Sorescu, D.C.; Kotchey, G.P.; Star, A. Chemical sensitivity of graphene edges decorated with metal nanoparticles. *Nano Lett.* **2011**, *11*, 2342–2347. [CrossRef]

35. Jung, M.W.; Kang, S.M.; Nam, K.-H.; An, K.-S.; Ku, B.-C. Highly transparent and flexible $NO_2$ gas sensor film based on $MoS_2$/rGO composites using soft lithographic patterning. *Appl. Surf. Sci.* **2018**, *456*, 7–12. [CrossRef]

36. Xian, L.; Jing, W.; Dan, X.; Xu, J.; Yi, X.; Lan, X.; Komarneni, S. Reduced graphene oxide/$MoS_2$ hybrid films for room-temperature formaldehyde detection. *Mater. Lett.* **2016**, *189*, 42–45.

37. Radisavljevic, B.; Radenovic, A.; Brivio, J.; Giacometti, V.; Kis, A. Single-layer $MoS_2$ transistors. *Nat. Nanotechnol.* **2011**, *6*, 147–150. [CrossRef]

38. Ganatra, R.; Zhang, Q. Few-Layer $MoS_2$: A Promising Layered Semiconductor. *ACS Nano* **2014**, *8*, 4074–4099. [CrossRef]

39. Zhu, X.; Zhu, Y.; Murali, S.; Stoller, M.D.; Ruoff, R.S. Nanostructured Reduced Graphene Oxide/$Fe_2O_3$ Composite as a High-Performance Anode Material for Lithium Ion Batteries. *ACS Nano* **2011**, *5*, 3333–3338. [CrossRef]

40. Zu, S.Z.; Han, B.H. Aqueous Dispersion of Graphene Sheets Stabilized by Pluronic Copolymers: Formation of Supramolecular Hydrogel. *J. Phys. Chem. C* **2009**, *113*, 13651–13657. [CrossRef]

41. Shao, L.; Wu, Z.; Duan, H.; Shaymurat, T. Discriminative and rapid detection of ozone realized by sensor array of $Zn^{2+}$ doping tailored $MoS_2$ ultrathin nanosheets. *Sens. Actuators B Chem.* **2018**, *258*, 937–946. [CrossRef]

42. Chen, X.; Meng, D.; Wang, B.; Li, B.W.; Li, W.; Bielawski, C.W.; Ruoff, R.S. Rapid thermal decomposition of confined graphene oxide films in air. *Carbon* **2016**, *101*, 71–76. [CrossRef]

43. Zhang, J.; Lu, H.; Yan, C.; Yang, Z.; Zhu, G.; Gao, J.; Yin, F.; Wang, C. Fabrication of conductive graphene oxide-WO$_3$ composite nanofibers by electrospinning and their enhanced acetone gas sensing properties. *Sens. Actuators B Chem.* **2018**, *264*, 128–138. [CrossRef]

44. Li, Q.; Guo, B.; Yu, J.; Ran, J.; Zhang, B.; Yan, H.; Gong, J.R. Highly efficient visible-light-driven photocatalytic hydrogen production of CdS-cluster-decorated graphene nanosheets. *Am. Chem. Soc.* **2011**, *133*, 10878–10884. [CrossRef]

45. Niu, Y.; Wang, R.; Jiao, W.; Ding, G.; Hao, L.; Yang, F.; He, X. MoS$_2$ graphene fiber based gas sensing devices. *Carbon* **2015**, *95*, 34–41. [CrossRef]

46. Ghasemi, F.; Jalali, M.; Abdollahi, A.; Mohammadi, S.; Sanaee, Z.; Mohajerzadeh, S. A high performance supercapacitor based on decoration of MoS$_2$/reduced graphene oxide with NiO nanoparticles. *RSC Adv.* **2017**, *7*, 52772–52781. [CrossRef]

47. Lipatov, A.; Varezhnikov, A.; Wilson, P.; Sysoev, V.; Kolmakov, A.; Sinitskii, A. Highly selective gas sensor arrays based on thermally reduced graphene oxide. *Nanoscale* **2013**, *5*, 5426–5434. [CrossRef]

48. Kumar, R.; Goel, N.; Kumar, M. High performance NO$_2$ sensor using MoS$_2$ nanowires network. *Appl. Phys. Lett.* **2018**, *112*, 053502. [CrossRef]

49. Saraf, M.; Natarajan, K.; Saini, A.K.; Mobin, S.M. Small biomolecule sensors based on an innovative MoS$_2$-rGO heterostructure modified electrode platform: A binder-free approach. *Dalton Trans.* **2017**, *46*, 15848–15858. [CrossRef]

50. Li, H.; Yu, K.; Li, C.; Tang, Z.; Guo, B.; Lei, X.; Fu, H.; Zhu, Z. Charge-Transfer Induced High Efficient Hydrogen Evolution of MoS$_2$/graphene Cocatalyst. *Sci. Rep.* **2015**, *5*, 18730. [CrossRef]

51. Lu, Y.; Meyyappan, M.; Li, J. Trace detection of hydrogen peroxide vapor using a carbon-nanotube-based chemical sensor. *Small* **2011**, *7*, 1714–1718. [CrossRef]

52. Lee, D.J.; Choi, S.W.; Byun, Y.T. Room temperature monitoring of hydrogen peroxide vapor using platinum nanoparticles-decorated single-walled carbon nanotube networks. *Sens. Actuators B Chem.* **2017**, *256*, 744–750. [CrossRef]

53. Verma, A.L.; Saxena, S.; Saini, G.S.S.; Gaur, V.; Jain, V.K. Hydrogen peroxide vapor sensor using metal-phthalocyanine functionalized carbon nanotubes. *Thin Solid Films* **2011**, *519*, 8144–8148. [CrossRef]

54. Lichtenstein, A.; Havivi, E.; Shacham, R.; Hahamy, E.; Leibovich, R.; Pevzner, A.; Krivitsky, V.; Davivi, G.; Presman, I.; Elnathan, R. Supersensitive fingerprinting of explosives by chemically modified nanosensors arrays. *Nat. Commun.* **2014**, *5*, 4195. [CrossRef]

55. Wu, Z.; Zhou, C.; Zu, B.; Li, Y.; Dou, X. Contactless and Rapid Discrimination of Improvised Explosives Realized by Mn$^{2+}$ Doping Tailored ZnS Nanocrystals. *Adv. Funct. Mater.* **2016**, *26*, 4578–4586. [CrossRef]

56. Abdi, H.; Williams, L.J. Principal component analysis. *Wiley Interdiscip. Rev. Comput. Stat.* **2010**, *2*, 433–459. [CrossRef]

57. Jolliffe, I.T. Principal component analysis. *J. Mark. Res.* **2002**, *87*, 513.

58. Lu, Y.; Partridge, C.; Meyyappan, M.; Jing, L. A carbon nanotube sensor array for sensitive gas discrimination using principal component analysis. *J. Electroanal. Chem.* **2006**, *593*, 105–110. [CrossRef]

59. Li, J.; Liu, Y.; Zhang, J.; Liang, X.; Duan, H. Density functional theory study of the adsorption of hydrogen atoms on Cu$_{2X}$ (X = 3d) clusters. *Chem. Phys. Lett.* **2016**, *651*, 137–143. [CrossRef]

60. Bhati, V.S.; Ranwa, S.; Rajamani, S.; Kumari, K.; Raliya, R.; Biswas, P.; Kumar, M. Improved sensitivity with low limit of detection of hydrogen gas sensor based on rGO loaded Ni doped ZnO nanostructures. *ACS Appl. Mater. Interfaces* **2018**, *10*, 11116–11124. [CrossRef]

61. Näther, N.; Henkel, H.; Schneider, A.; Schöning, M.J. Investigation of different catalytically active and passive materials for realising a hydrogen peroxide gas sensor. *Phys. Status Solidi* **2010**, *206*, 449–454. [CrossRef]